nanomaterials

MDPI

Article

Prediction of gold nanoparticle and microwave-induced hyperthermia effects on tumor control via a simulation approach

Nikolaos M. Dimitriou[a,d], Athanasia Pavlopoulou[b], Ioanna Tremi[a], Vassilis Kouloulias[c], Alexandros G. Georgakilas[a,*]

[a] DNA Damage Laboratory, Department of Physics, School of Applied Mathematical and Physical Sciences, National Technical University of Athens (NTUA), Zografou Campus, 15780 Athens, Greece. E-mail: alexg@mail.ntua.gr, nikolaos.dimitriou@mail.mcgill.ca, ioannatremi@mail.ntua.gr

[b] Izmir International Biomedicine and Genome Institute, Dokuz Eylül University, 35340, Turkey. E-mail: athanasia.pavlopoulou@deu.edu.tr

[c] Radiation Oncology Unit, 2nd Department of Radiology, Attikon University General Hospital, Medical School, National and Kapodistrian University of Athens, Athens, Greece. E-mail: vkouloul@ece.ntua.gr

[d] Department of Bioengineering, McGill University, Montreal, Quebec, Canada. E-mail: nikolaos.dimitriou@mail.mcgill.ca

[*] Corresponding author: Alexandros Georgakilas. alexg@mail.ntua.gr

Abstract: Hyperthermia acts as a powerful adjuvant to radiation therapy and chemotherapy. Recent advances show that gold nanoparticles (Au-NPs) can serve as unique mediators of highly localized thermal effects upon interaction with laser radiation. The purpose of this study was to investigate via *in silico* simulations the mechanisms of Au-NPs and microwave-induced hyperthermia, in correlation to predictions of tumor control (tumor shrinkage and cell death) after hyperthermia treatment. To this end, we calculated the hyperthermia effect for two types of Au-NPs and two types of spherical tumors (prostate and melanoma) with a radius of 3 mm. The plasmon peak for the 30 nm Si-core Au-coated NPs was found at 590 nm and for the 20 nm AuNPs at 540 nm. Considering the plasmon peaks and the distribution of NPs in the tumor tissue, the induced thermal profile was estimated for different intervals of time. Predictions of hyperthermic cell death were performed by adopting a Three-State Mathematical Model, where "three-state" includes i) alive, ii) vulnerable and iii) dead states of the cell and it is coupled with a tumor growth model. Our proposed methodology and preliminary results could be considered as a proof-of-principle for the significance of simulating accurately the hyperthermia-based tumor control. We also propose a method for the optimization of treatment by overcoming thermoresistance by biological means and specifically through the targeting of the heat shock protein 90 (HSP90), which plays a critical role in the thermotolerance of cells and tissues.

Keywords: Hyperthermia; gold nanoparticles; simulation; thermoresistance; tumor control

1. Introduction

Although, great advances have been made in early diagnosis and treatment of cancer, it remains one of the leading causes of death worldwide. Radiotherapy and chemotherapy represent the main modalities of cancer treatment. However, a great number of cancer patients develop side effects, thereby making these treatments painful and very unpleasant due to the intrinsic sensitivity of the adjacent normal tissue [1]. As a result, targeted therapies are becoming increasingly urgent because they can minimize any side effects and make the treatment more efficient. Even though hyperthermia does not stand on the front line of cancer therapy, historical evidence suggest that thermal therapy was used in ancient times, as Hippocrates stated "*what medicines do not heal, the lance will; what the*

lance does not heal, fire will" [2]. Hyperthermia, with or without enhancement of its effects by gold nanoparticles (Au-NPs), has the potential of eliminating the disastrous side effects of traditional cancer therapies acting primarily as an adjuvant to radiation or chemotherapy [3]. Metallic nanoparticles, like gold, strongly absorb and scatter light close to their localized surface plasmon resonance (LSPR) and therefore can be used as heat emitters. As a result, they convert electromagnetic energy into heat thereby causing hyperthermic cell damage [4]. Heat delivered within the hyperthermia range (42-48 ºC) induces tumor cell death, primarily by denaturation of essential cellular proteins [5].

Different kinds of cell death correspopnd to different immune responses. Apoptotic cancer cells are suggested to stimulate tumor cell repopulation and induce immunological silence or tolerance [6]. In contrast, cancer cells in response to certain anticancer treatments, including cytostatic drugs, radiotherapy or application of heat above 47 ºC for up to 10 minutes, the so called "thermal ablation" range, undergo necrosis or necroptosis, that is, immunogenic cell death (ICD) [7]. ICD possesses immunogenic potential, leading to the release of immunostimulatory factors and endogenous molecules, referred to as disease-associated molecular patterns (DAMPs), to the extracellular milieu, capable of priming an effective cancer-specific immune response, thereby leading to the destruction of any surviving, therapy-resistant cancer cells and the development of immune memory [8]. This cell debris binds to the cognate receptors of innate immune cells such as dendritic cells (DC) to stimulate their maturation into professional antigen-presenting cells (APCs) and consequently activates $CD4^+$ $CD8^+$ T lymphocytes by DC-mediated antigen presentation. In addition, ICD is associated with increased infiltration of lymph nodes by B cells which produce tumor-specific antibodies [9]. Hyperthermia inhibits also DNA repair, including proper processing and amendment of double-strand breaks (DSBs), making it a potent radio- and chemosensitizer, for various types of cancer, including tumors of head and neck, bladder, breast and cervix [8].

However, cells utilize an evolutionarily conserved defense mechanism which renders them thermotolerant, the so called heat shock response, where molecular chaperones such as heat shock proteins (HSPs) bind to client proteins denatured by heating in order to mediate their proper folding, their transport into organelles or their proteosomal degradation [10]. For example, it has been shown that HSP90 inhibitor Ganetespib enhances the cytotoxic effects of hyperthermia, with or without radio- or chemotherapy, and decreases thermotolerance in cervix cancer cell lines [8]. At the transcriptoanal level, heat-activated heat shock factor 1 (HSF1) in mammals induce the expression of genes encoding HSPs (e.g., HSP70 and HSP90) [11]. Of importance, extracellular or membrane bound HSPs (e.g., HSP90) can also act as DAMPs, without contributing to the immunogenic potential of necrotic cancer cells though [12].

In the first part of our study we investigate the effect of the size, shape and structure of the nanoparticles on their absorption efficiency for the optical spectrum. This simulation involves the calculation of absorption cross-section of spherical particles and nanoshells using Mie's theory [9]. The nanoparticles that are investigated have spherical, with diameters from 10 nm to 1000 nm, and ellipsoid shape and their structure involves gold (bulk), silica core with gold in the outer layer and golden core with TiO_2 outer layer.

In the second part of our study, we present a simulation framework of tumor response during hyperthermia treatment mediated by laser and Au-NPs, and hyperthermia induced by microwaves without the contribution of the nanoparticles. The primary goal of this study was to obtain the thermal profiles for the two types of spherical tumors and estimate the extend of tumor shrinkage. In the first form of thermal therapy (laser-induced hyperthermia with Au-NPs) we predicted the optimal radiation wavelength based on nanoparticles' selected sizes and material type. Then, we computed the thermal profile both in the tumorous and the surrounding healthy tissue for a given nanoparticle distribution in the tissue. In the second form of therapy we investigated the thermal distribution produced by an antenna tuned in varying microwave frequencies. By using a three-state mathematical model of hyperthermic cell death [13], an exponential tumor growth model [14] and calibration of models against experimental data, we obtained a long-term evolution of tumor size for

96 melanoma and prostate cancer. In addition, we demonstrated enhanced tumor shrinkage upon
97 HSP90 inhibition. The tumors are considered spherical with a radius approximately 3 mm.

98 **2. Materials and Methods**

99

100 *2.1 Effect of the size, shape and structure of the nanoparticles on their absorption efficiency*

101 In this section we performed a detailed study of the dependence of the absorption efficiency of
102 nanoparticles on their size, shape and structure. The absorption and scattering cross section of a
103 spherical particle can be calculated using Mie's theory [9], which has also been applied in the case of
104 nanoshells [15], i.e. nanoparticles in the form of two concentric spheres with different materials in the
105 inner and outer layer. According to this theory, the absorption efficiency of a nanoshell, namely the
106 ratio of the absorption cross section to the geometrical cross section is given by the formula

$$Q_{abs} = \frac{2}{x_2^2}\sum_{n=1}^{\infty}(2n+1)\left(\mathrm{Re}\left[a_n + b_n\right] - |a_n|^2 - |b_n|^2\right) \quad (1)$$

107
108 Where

$$a_n = \frac{\psi_n(x_2)\left[\psi_n'(m_2x_2) - A_n\chi_n'(m_2x_2)\right] - m_2\psi_n'(x_2)\left[\psi_n(m_2x_2) - A_n\chi_n(m_2x_2)\right]}{\xi_n(x_2)\left[\psi_n'(m_2x_2) - A_n\chi_n'(m_2x_2)\right] - m_2\xi_n'(x_2)\left[\psi_n(m_2x_2) - A_n\chi_n(m_2x_2)\right]} \quad (2)$$

109

$$b_n = \frac{m_2\psi_n(x_2)\left[\psi_n'(m_2x_2) - B_n\chi_n'(m_2x_2)\right] - \psi_n'(x_2)\left[\psi_n(m_2x_2) - B_n\chi_n(m_2x_2)\right]}{m_2\xi_n(x_2)\left[\psi_n'(m_2x_2) - B_n\chi_n'(m_2x_2)\right] - \xi_n'(x_2)\left[\psi_n(m_2x_2) - B_n\chi_n(m_2x_2)\right]} \quad (3)$$

110 and

$$A_n = \frac{m_2\psi_n(m_2x_1)\psi_n'(m_1x_1) - m_1\psi_n'(m_2x_1)\psi_n(m_1x_1)}{m_2\chi_n(m_2x_1)\psi_n'(m_1x_1) - m_1\chi_n'(m_2x_1)\psi_n(m_1x_1)} \quad (4)$$

111

$$B_n = \frac{m_2\psi_n(m_1x_1)\psi_n'(m_2x_1) - m_1\psi_n'(m_1x_1)\psi_n(m_2x_1)}{m_2\chi_n'(m_2x_1)\psi_n(m_1x_1) - m_1\chi_n(m_2x_1)\psi_n'(m_1x_1)} \quad (5)$$

112

113 Here $m_1 = n_1/n_m, m_2 = n_2/n_m$, $x_1 = 2\pi R_1 n_m/\lambda, x_2 = 2\pi R_2 n_m/\lambda$ and
114 $\psi_n(\rho) = \rho j_n(\rho), \chi_n(\rho) = -\rho y_n(\rho), \xi_n(\rho) = \rho h_n^{(1)}(\rho)$, where n_1, n_2, n_m are the complex
115 refractive indices of the inner layer, the outer layer and the surrounding medium, respectively;
116 R_1, R_2 are the radii of the inner and outer layer respectively, λ is the wavelength of the incident
117 radiation in vacuum and $j_n, y_n, h_n^{(1)}$ are the spherical Bessel functions of the first, second and third
118 kind respectively. These equations can be easily simplified to the case of a single layer spherical
119 nanoparticle setting $A_n = B_n = 0$.

120 Further, the dielectric constant $\varepsilon(\omega)$ of small metal particles was modified taking into
121 consideration the scattering of free electrons on the surface of the nanoparticle. Thus, it takes the form
122 [16]

$$\varepsilon\left(\omega, L_{eff}\right) = \varepsilon_{bulk}\left(\omega\right) + \frac{\omega_p^2}{\omega^2 + i\omega\upsilon_F / L_\infty} - \frac{\omega_p^2}{\omega^2 + i\omega\left(\upsilon_F / L_\infty + A\upsilon_F / L_{eff}\right)} \quad (6)$$

where ω is the angular frequency of the incident radiation, L_{eff} is the reduced mean free path length of free electrons, $\varepsilon_{bulk}\left(\omega\right)$ the dielectric constant of the bulk material, ω_p the plasma angular frequency, υ_F the Fermi velocity, L_∞ the mean free path length of free electrons, and A a dimensionless constant which is usually assumed to be close to unity. The values of these constants for gold are usually taken as [17] $\omega_p = 1.37\times10^{16}\ rad/s$, $\upsilon_F = 1.4\times10^{6}\ m/s$, $L_\infty = 4.2\times10^{-8} m$, and $A = 1$. On the other hand, L_{eff} is set equal to the thickness of the gold layer. The dielectric constants of the bulk materials, as well as the surrounding medium, are measured through a reliable online database [18].

First, we consider the effect of the particle size on its absorption cross section. As shown in **Figure 1**, the absorption cross section of the nanoparticles increases relatively to their diameter. However, the peak of the absorption cross section does not change significantly and remains in the region of 500 nm.

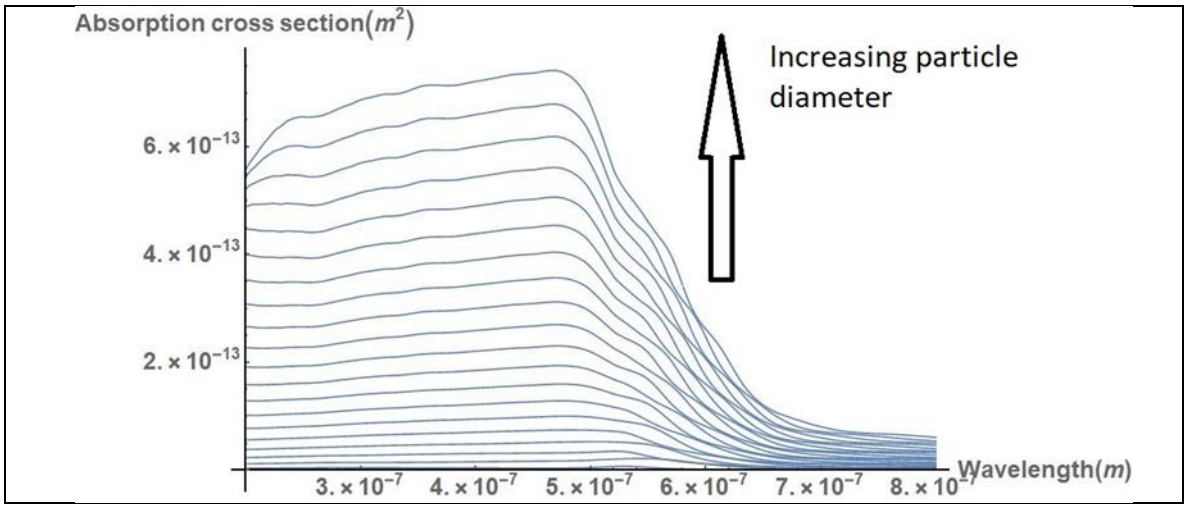

Figure 1. Absorption spectra of gold nanoparticles of different diameters (10 nm – 1000 nm). The cross section increases, but the peak lies in the region of 500 nm for all curves.

From **Figure 2**, it is deduced that the absorption cross section of the gold nanoparticles increases inversely with their diameter $\sim d^P$ where the exponent p is of the order of 1.5. This finding shows that for larger nanoparticles the absorption cross section does not increase as rapidly with their size as in the case of small nanoparticles, where according to the dipole approximation, the absorption cross section increases $\sim d^3$.

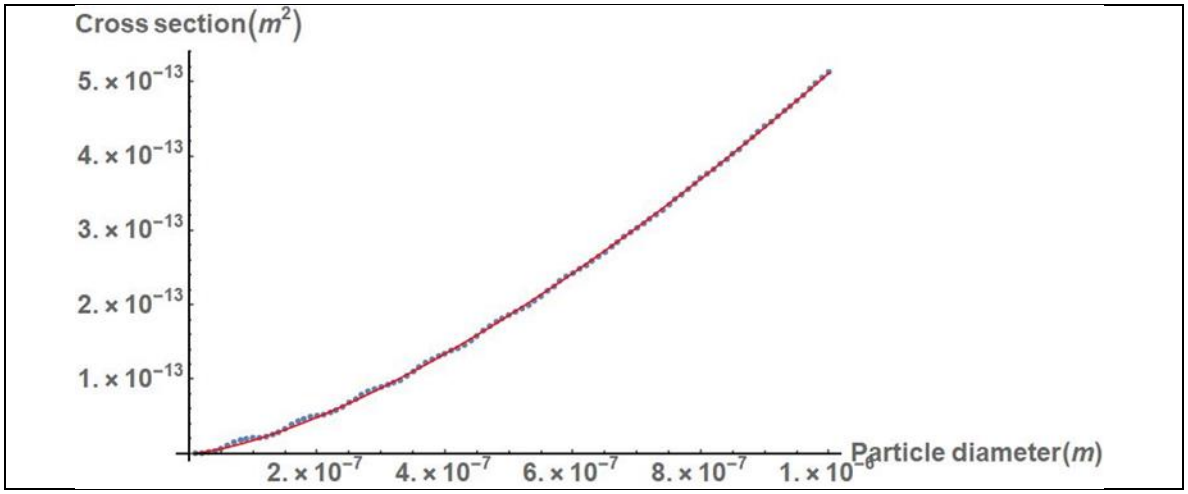

Figure 2. The absorption cross section of gold nanoparticles as a function of their diameter. The red line is a fitting curve based on the function $y = \alpha x^p$, where $\alpha = 2.9\times10^{-4}$ and $p = 1.46$. The incident wavelength is assumed to be 532 nm, which is a common laser wavelength corresponding to the second harmonic of Nd: YAG lasers, and it is also in the region of maximum absorption of gold nanoparticles.

We have also studied the behavior of the absorption efficiency of a nanoshell consisting of a silica core surrounded by a gold layer, as in the case of the hyperthermia simulations. From **Figure 3** the absorption spectrum of the nanoshell is red-shifted as the thickness of the gold layer decreases.

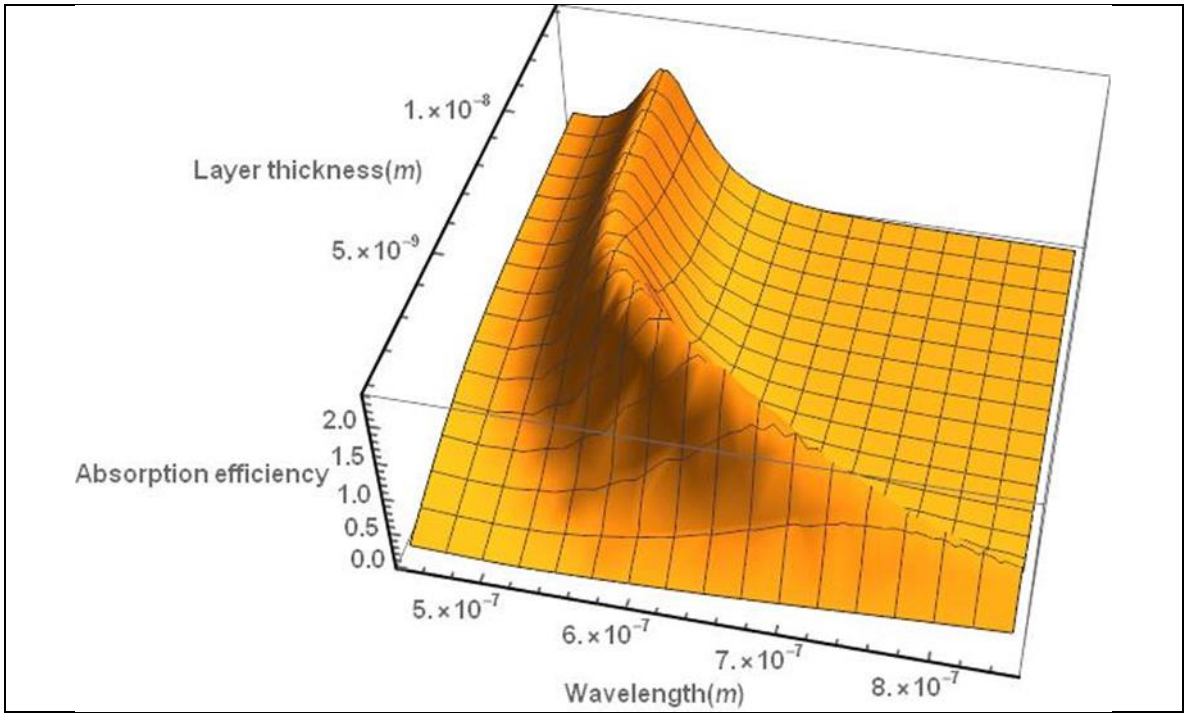

Figure 3. Absorption efficiency spectrum of a gold nanoshell as a function of the thickness of the gold layer. The spectrum is red-shifted as the nanoshell thickness decreases. The particle diameter is assumed to be 30 nm, as in the case of the hyperthermia simulations.

The absorption spectrum can also be red shifted by covering the gold nanoparticle with an appropriate layer of dielectric material, e.g. a TiO_2 layer, as shown in **Figure 4**.

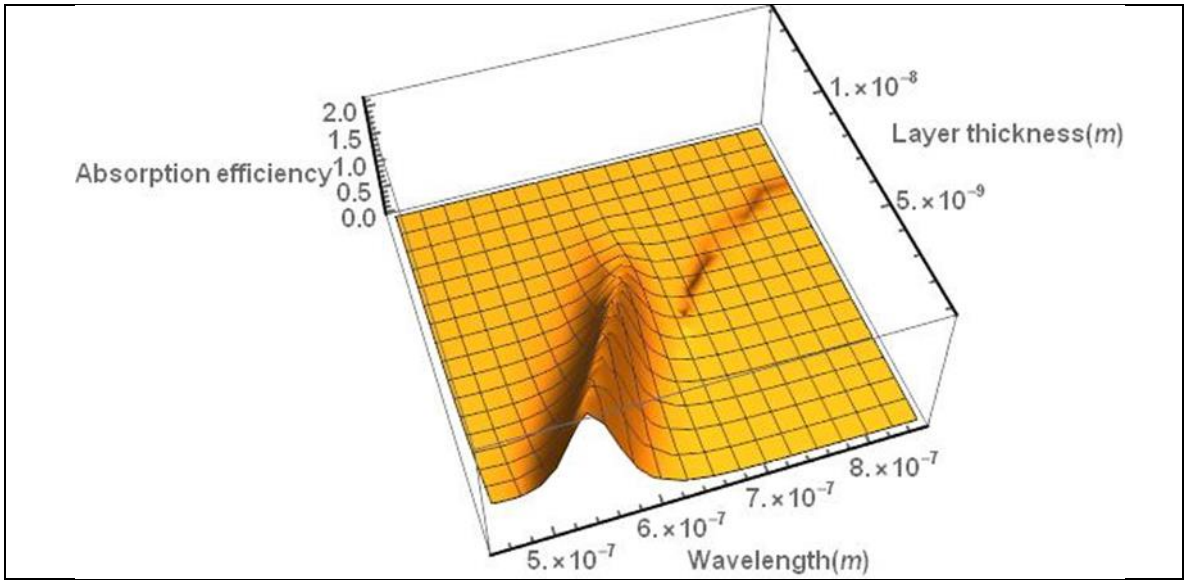

Figure 4. Absorption efficiency spectrum of a gold nanoparticle covered with a TiO_2 layer as a function of the thickness of the titania layer. The spectrum is red-shifted as the thickness of the dielectric layer increases. The particle diameter is assumed to be 30 nm.

Another way to red-shift the absorption spectrum of Au-NPs is by modifying their shape. Specifically, according to Gann's theory [19], the absorption cross section of a non-spherical nanoparticle having the form of a prolonged ellipsoid is given by the formula

$$\gamma_{abs} = \frac{2\pi V \varepsilon_m^{3/2}}{3\lambda} \sum_j \frac{\left(1/P_j^2\right)\varepsilon_2}{\left(\varepsilon_1 + \frac{1-P_j}{P_j}\varepsilon_m\right)^2 + \varepsilon_2^2} \tag{7}$$

where V is the volume of the nanoparticle, ε_m the dielectric constant of the surrounding medium, λ the wavelength of the incident radiation in vacuum, and $\varepsilon_1, \varepsilon_2$ the real and imaginary part of the dielectric constant of the nanoparticle respectively. The parameters P_j, often referred to as depolarization factors, are given by the formulas

$$P_A = \frac{1-e^2}{e^2}\left[\frac{1}{2e}\ln\left(\frac{1+e}{1-e}\right) - 1\right] \tag{8}$$

$$P_B = P_C = \frac{1-P_A}{2} \tag{9}$$

where

$$e = \sqrt{1-\frac{1}{r^2}}, \quad r = \frac{\ell_A}{\ell_B} \tag{10}$$

Here $\ell_A > \ell_B = \ell_C$ are the lengths of the principal semi axes of the ellipsoid. As shown in **Figure 5**, the absorption cross section of the nanoparticle increases and red-shifts significantly as the ratio of the principal semi axes increases.

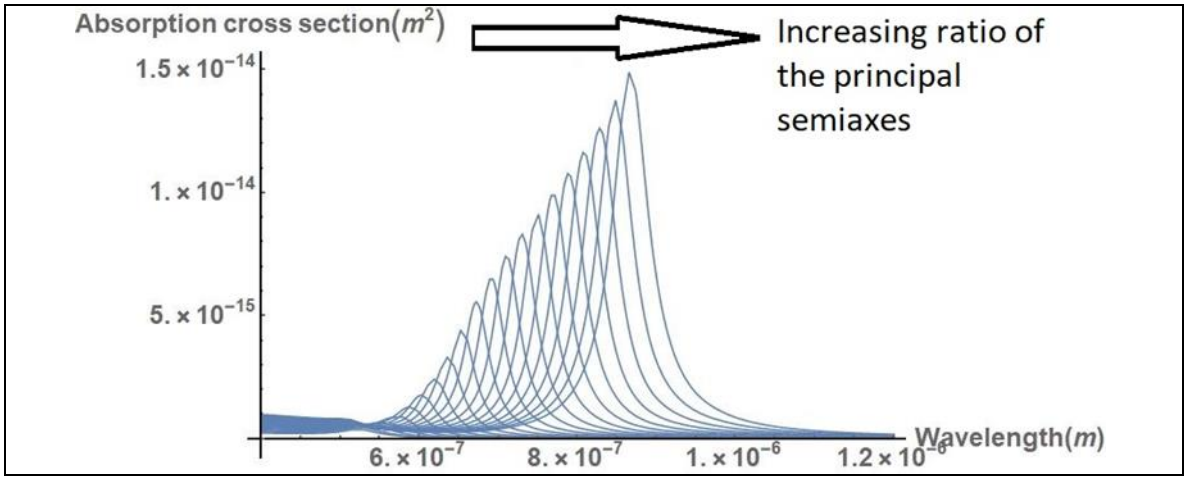

Figure 5. Absorption cross section of a gold nanoparticle in the form of a prolonged ellipsoid, for different values of the ratio of the principal semi axes $(1 \le r \le 5)$. The cross section is increased and red-shifted as the ratio of the principal axes increases.

Based on the above analysis the absorption spectrum of the nanoparticles can be tailored to meet the needs of specific applications, either by using a layered structure, or altering the shape of the nanoparticles.

2.2 Simulations for Nanoparticle and Microwave induced Hyperthermia and Hyperthermic Cell Death

In this part we present a novel study the aim of which is to calculate the tumor response under hyperthermic conditions. To this end, we tested two methods of thermal treatment. The first method is the Nanoparticle-induced hyperthermia and the second method is the traditional Microwave-induced hyperthermia. The pipelines that we followed for this study are synopsized in Figures 6(a), (b).

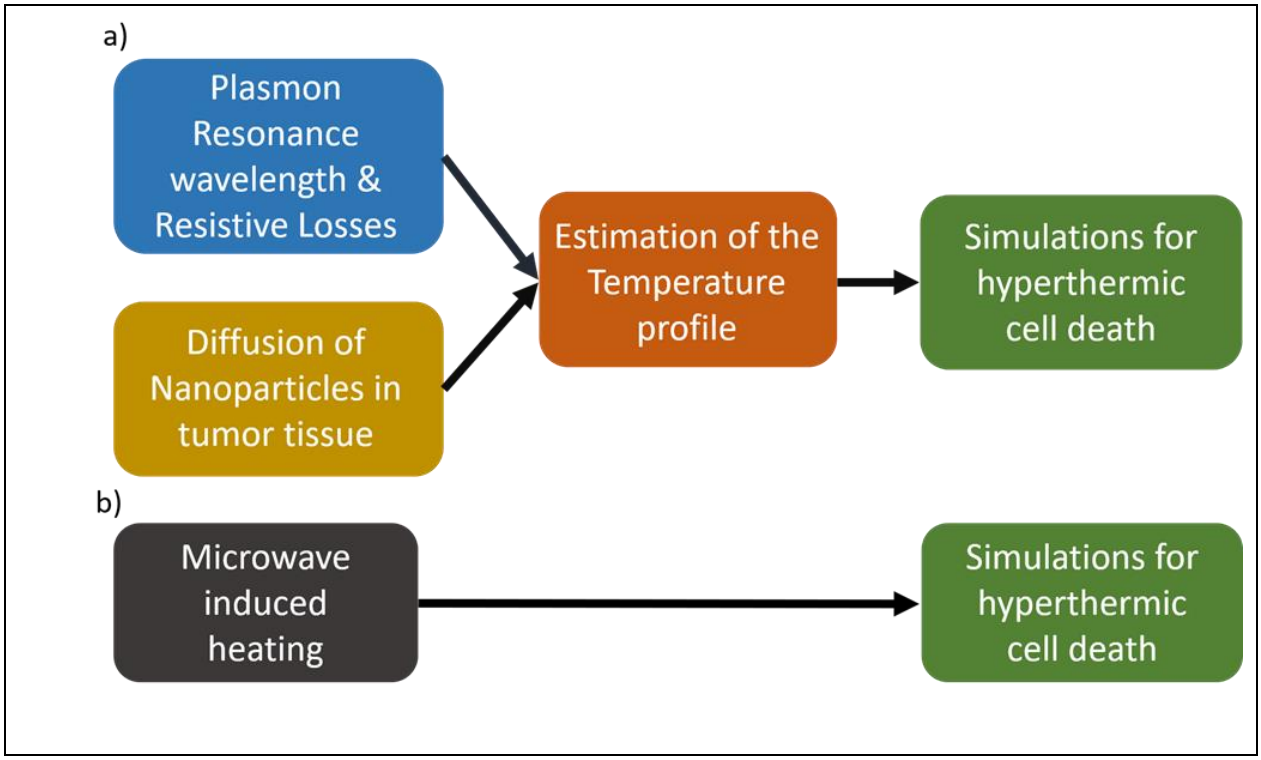

Figure 6. Workflow for the estimation of tumor shrinkage using: (**a**) gold nanoparticle induced hyperthermia and (**b**) using microwave induced hyperthermia.

2.3 Nanoparticle-induced hyperthermia

The first part of the study is focused on the prediction of the thermal profile inside the tumor. The simulations have been developed and formulated in Comsol 5.2 simulation software environment (www.comsol.com). The simulation was divided broadly into two major steps. The first part involves the search of the optimum wavelength in which the nanoparticles maximize the heat absorption. Two types of nanoparticles were investigated. The first type is a spherical gold nanoparticle with a diameter of 40 nm (**Figure 7(a), (c)**). The second type of nanoparticle has a silica core with a diameter of 20 nm and it is coated with gold 5 nm thick (**Figure 7(b), (d**)). The density power of the incoming laser beam was set at 20 W/cm^2. The beam is considered as a continuous wave (CW) and the incoming wave is plane. Water was set as the surrounding environment for both types of nanoparticles. The optical properties of gold are retrieved from Rakic [20], while the silica is taken by the built in library of Comsol.

$$\nabla \times (\nabla \times \boldsymbol{E}) - k_0^2 \varepsilon_r \boldsymbol{E} = 0 \quad (11)$$

The scattering boundary condition on the surface of nanoparticles are defined from the equation:

$$\mathbf{n} \times (\nabla \times (\boldsymbol{E} + \boldsymbol{E_b})) - (jk + 1/r)\mathbf{n} \times (\boldsymbol{E} \times \mathbf{n}) = 0 \quad (11a)$$

The eq. (11) describes the scattering of an incoming plane electromagnetic field, $\boldsymbol{E}(r, \varphi, z) = \widetilde{\boldsymbol{E}}(r, z)e^{-im\varphi}$, in the surface of a nanoparticle and $\varepsilon_r = (n' - jn'')^2$ is the complex valued relative permittivity calculated from the refractive index $n = n' - jn''$ of each material, k_0 is the free space wavenumber. Finally, in the eq. (11a) **n** is the vector perpendicular to surface of the nanoparticle and $\boldsymbol{E}_b = \boldsymbol{E}e^{-ik_0 x}$ is the background electric field.

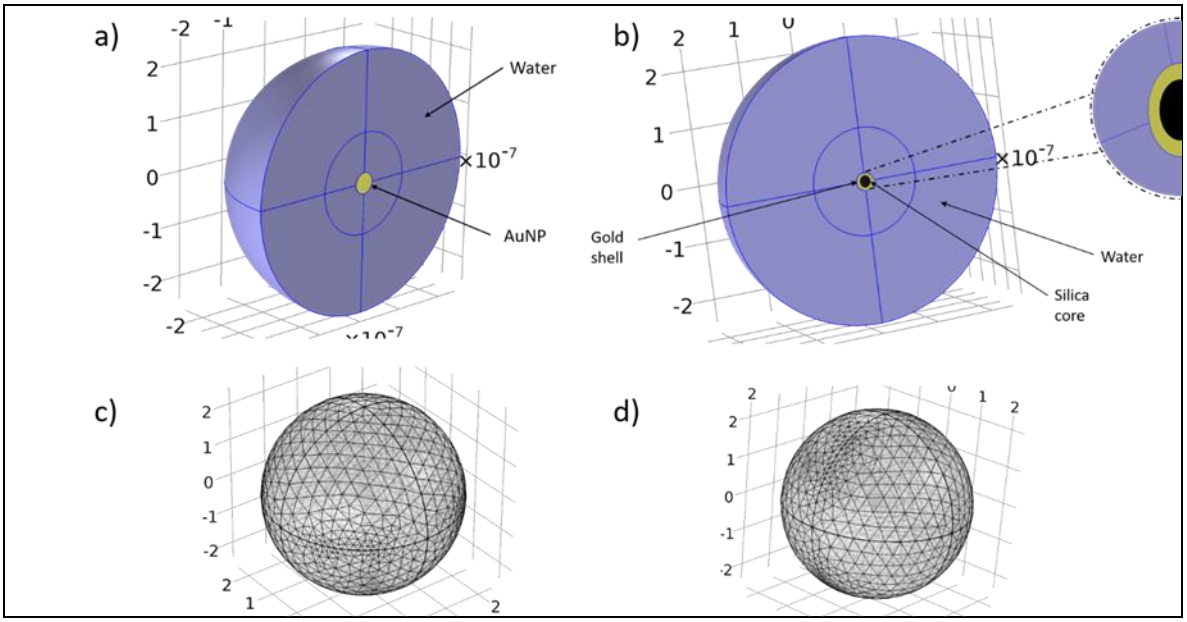

Figure 7. Corresponding geometries and meshes for the simulation of Plasmon Resonance. In (**a**) and (**c**) AuNP with 40 nm diameter surrounded by 225nm of water and in (**b**) and (**d**) AuSiO2NP with 30 nm diameter (20 nm SiO_2, 5 nm Au layer) surrounded by 225 nm of water.

In the second part, the laser radiation was applied in the tumor region, where a solution of nanoparticles was injected and diffused in the tissue and the thermal profile was obtained. The equations that were used for simulation are the following:

$$\frac{\partial c_i}{\partial t} + \quad \nabla \cdot (-D_i \nabla c_i) = R_i \tag{12}$$

$$\rho C_p \boldsymbol{u} \nabla \mathrm{T} + \quad \nabla \mathbf{q} = \mathrm{Q} + \quad Q_{bio} \tag{13}$$

$$Q_{bio} = \rho_b C_{p,b} \omega_b (T_b - T) + Q_{met} \tag{14}$$

Moreover, eq. (12) describes the diffusion of the injected nanoparticles solution inside the tumor tissue, where c_i is the variable of concentration of the nanoparticles, D_i is the diffusion coefficient of each material and R_i is a generation term which was set at 30 nanoparticles/m³s. The concentration of NPs injected into the tumor is 40 μg/ml [21]. The solution is injected into the center of the tumor. The last equations, eq. (13) and (14), represent the diffusion of the heat produced by the nanoparticles, inside the tumor and the surrounding region, where $\boldsymbol{q} = -k\nabla T$ (k the thermal conductivity), $\boldsymbol{u}$ the normal vector, ρ and ρ_b are the densities of each tissue and blood respectively, C_p, and $C_{p,b}$ the specific heat capacities of tissues and blood, T and T_b the temperatures of tissue and arterial blood, ω_b the blood perfusion rate, Q_{met} the metabolic heat source. The values of the various parameters are presented in **Table 2**.

The results are also compared with microwave-induced hyperthermia for both melanoma and prostate cancer. In this study, we used the same theoretical background for electromagnetic scattering, but different geometries that include the transrectal microwave antenna for the prostate (**Figure 8**) and an antenna that is in contact with the skin for the melanoma (**Figure 9**). Both antennas are operating in 433 MHz and 2.4 GHz.

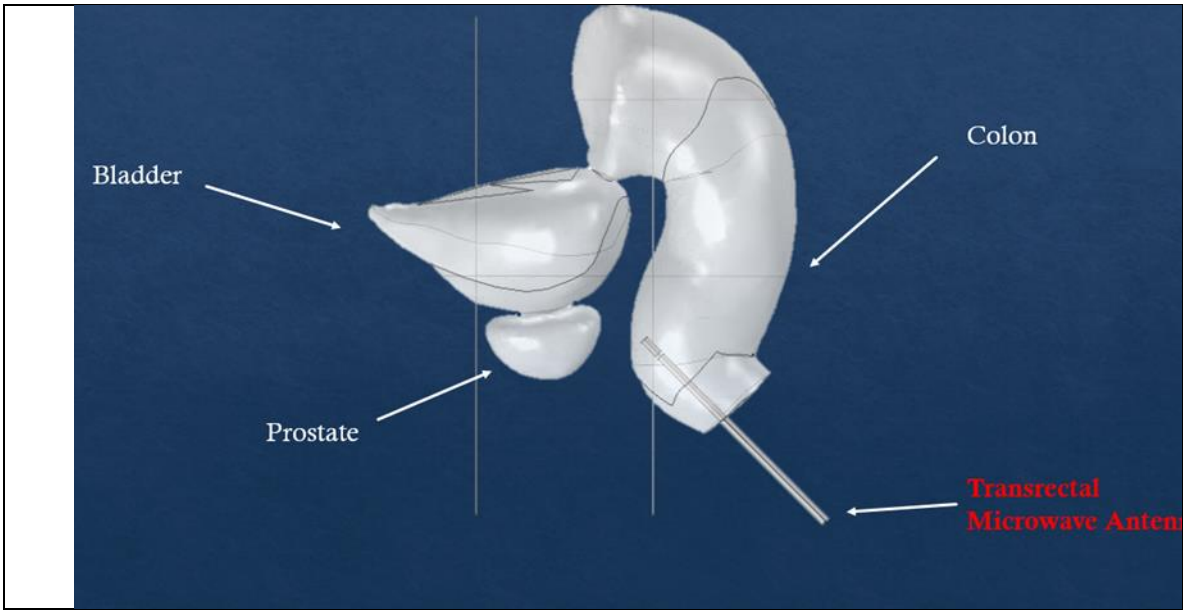

242 **Figure 8.** Simulated scenario of microwave-induced hyperthermia for prostate cancer.

243 **Figure 9.** Simulated scenario of microwave induced hyperthermia for melanoma.

244 For the corresponding geometries, fine sized, free tetrahedral meshes for the nanoparticles and
245 normal sized, free triangular, and meshes for the melanoma and prostate geometries were selected.
246 Their characteristics are shown in **Table 1**.
247

248 **Table 1.** Parameters of the meshes for the corresponding geometries.

	AuNP 20 nm (surrounded by 225 nm of water) **(Figure 7(a), (c))**	$AuSiO_2$NP 30 nm (surrounded by 225 nm of water) **(Figure 7(b), (d))**	Melanoma **(Figure 9)**	Prostate (**Figure 12**)
Max element size	39.2 nm	38.4 nm	5.36 mm	5.36
Min element size	4.9 nm	4.8 nm	24 μm	24.5 μm
Max element growth rate	1.45	1.45	1.3	1.3
Curvature factor	0.5	0.5	0.3	0.3
Resolution of narrow regions	0.6	0.6	1	1

249 **Table 1.** Selected parameters for Blood, Dermis, Epidermis, Fat, Tumor and Muscles tissues as used
250 in equations (2-4).

	Specific heat capacity Cp (J/kg/°C)	**Density ϱ (kg/m³)**	**Thermal conductivity k (W/m·°C)**	**Blood perfusion rate w (m³/m³·s)**	**Metabolic heat source qm (W/kg)**	**Diffusivity m²/s**
Blood	3617 [22]	1050 [22]	0.52 [22]	-	1090 [23]	-
Dermis	3300 [24]	1200 [24]	0.45 [24]	1.25×10^{-3} [24]	1200 [25]	-
Epidermis	3590 [24]	1200 [24]	0.23 [24]	0 [24]	1200 [25]	6.2×10^{-11} [26]
Fat	2348 [22]	911 [22]	0.21 [22]	1.25×10^{-3} [24]	464 [25]	-
Tumor/ Muscle	3421 [22]	1090 [22]	0.49 [22]	1.65×10^{-3} [22]	991 [22]	

251 *2.4 Estimation of hyperthermic cell death*

252 The second part of the study concerns the prediction of the tumor response and specifically
253 tumor size during the days the patient received laser-induced hyperthermia treatment with Au-NPs.
254 In this part, the models that were used are i) a three-state mathematical model of hyperthermic cell
255 death [13] and ii) an exponential model of tumor growth [14]. The first model predicted the shrinkage
256 of the tumor due to hyperthermia treatment and the second one the growth of the tumor because of
257 the survived cells and their subsequent growing.
258 The prediction of hyperthermic cell death is thoroughly described in a study by O'Neil et al. [13],
259 where they present a Three-State Mathematical Model of Hyperthermic Cell Death in which the
260 "three-state" term stands for the i) alive, ii) vulnerable and iii) dead states of the cell. The benefits of
261 using this model is its flexibility of describing the cell death due to necrosis (fast cell death) and
262 apoptosis (slow-programmed cell death). The equations that are used are the following:

$$A + V + D = 1 \tag{15}$$

263

$$\frac{dA}{dt} = -k_f A + k_b(1 - A - D) \tag{16}$$

264

$$\frac{dD}{dt} = k_f(1 - A - D) \tag{17}$$

$$\frac{dD}{dt} = k_s(1 - D) \quad (18)$$

In the first equation (eq. 15), the three states of the cells are taken into consideration; *A* for alive, *V* for vulnerable, *D* for dead. Equations (16) and (17) describe the rates of the alive and dead cells during fast cell death. The parameter $k_f = \overline{k_f} e^{\frac{T}{T_k}}(1 - A)$ is a forward rate parameter, where $\overline{k_f}$ is a scaling constant, T_k sets the rate of exponential increase with temperature, *T* the temperature variable, and k_b a backward rate constant. The last equation, eq. (18), describes the rate changes of dead cells during slow cell death, where $k_s = \overline{k_s} D(1 - D)(D - D_\tau)^2$. The constants $\overline{k_s}$ is a baseline scaling value for k_s, and D_τ a threshold value of maximum cell death for cultures that have suffered minimal thermal damage. The parameters $\overline{k_f}$, k_b, T_k, k_s and D_τ are being estimated using the function "fmincon" that finds minimum of constrained nonlinear multivariable function, and is provided by MATLAB, and with experimental data from Blanco-Andujar et al. and Feng et al. [27] for melanoma, Huang et al. [28] for prostate cancer. The optimized parameters are presented in **Table 3**. In slow cell death, the cells are only needing to be considered either as "dead" or "not dead". As a result, in slow cell death, there is not a vulnerable phase and $k_f = k_b = 0$.

Table 2. Parameters for hyperthermic cell death model.

	Melanoma	Prostate cancer
Temperature (degrees Celsius)	48	50
$\overline{k_f}$ (min^{-1})	0.25481	0.18946
k_b (min^{-1})	0.66477	0.23063
T_k (degrees Celsius)	40.1513	39.678
$\overline{k_s}$ (hours^{-1})	0.59547	$0.316 * 10^{-3}$ (no data)
D_τ	$0.45003 * 10^{-3}$	0.208 (no data)

2.5 Tumor growth model

Besides the cell death model, the growth of tumor has been modeled with a simple exponential growth [14], when the effect of the treatment is over. The equation is the following:

$$\frac{dV}{dt} = a_0 V \quad (9)$$

Here, the coefficient a_0 is estimated from experimental data. The simple exponential model is calibrated against experimental data from Proia et al. [29] for melanoma and Gao et al. [30] for prostate cancer (**Table 4**). Proia et al. investigated, also, the melanoma growth differentiation upon HSP90 inhibition (**Figure 14**).

Table 3. Calibrated parameters for tumor growth model.

	Melanoma	Melanoma (HSP90 inhibited)	Prostate cancer
α_0 (s^{-1})	0.328 ± 0.003	0.237 ± 0.005	0.243 ± 0.016

3. Results

From the first simulation study, we observe in **Figure 10(a)** the wavelengths in which the LSPR effect is occurred. The plasmon peak for the Au-SiNP and AuNP is found at 590 nm and 540 nm, respectively. Experimental data show that the plasmon peak for AuNPs, with a diameter approximately 40nm, can be found at 535 nm [31]. Also, Sambou et al. [32] shows that for the (20nm diameter) Silica-core/(5nm thickness)Au-NPs can be found at around 600 nm. Moreover, we simulated the diffusion of nanoparticles inside the tumorous tissue. The tumor is considered spherical with a radius of approximately 3 mm and volume 113 mm^3. In the diffusion study, the NPs diffuse radially following a Gaussian form, outwards both tumorous ($r \leq 3$ mm) and the surrounding healthy tissue ($r>3$ mm), forming a concentration gradient (**Figure 10(b)**). The distribution of the NPs in the cancerous region should be in a way that the induced thermal effect would not damage the healthy tissue. Concluding the first part of our study, we have produced thermal profile of the tumorous and surrounding healthy tissue at the 10th minute of the heating procedure (**Figure 10(c)**). The intratumoral temperature surpasses the threshold of cell damage, while the temperature of the surrounding healthy tissue, between 3 mm and 6 mm, is, also, raised to a degree that can cause damage.

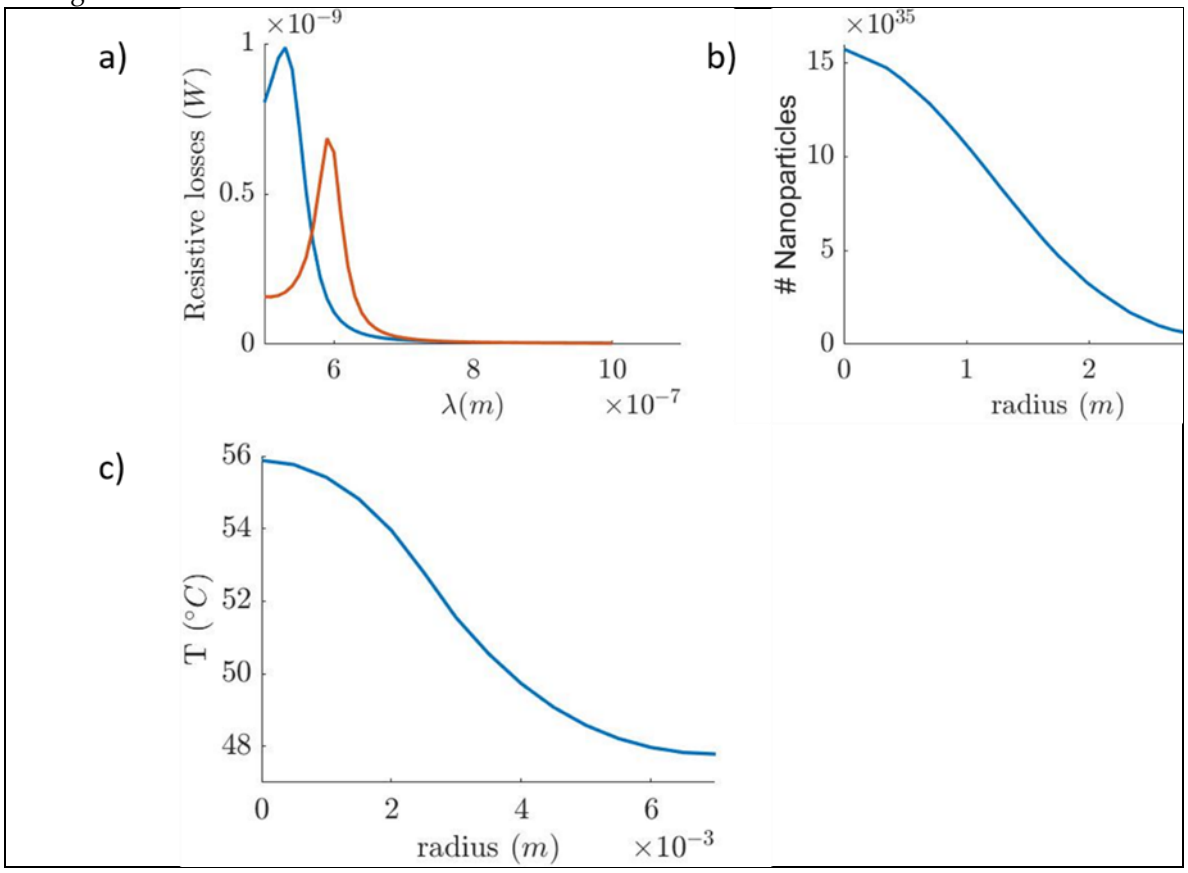

Figure 10. Resonant wavelength of two different size nanoparticles. (**a**) the blue line corresponds to the 40 nm AuNP and the orange line to the 30 nm Au-SiNP. (**b**) distribution of NPs inside the tumorous tissue 1 hour after the injection in the center of the tumor. (**c**) temperature rise during the first 10 minutes of NP laser-induced heating.

The temperature generated by the nanoparticle-based therapy appears to be sufficient for the eradication of the corresponding tumors. The differences between NP-induced and the traditional microwave-induced hyperthermia for the melanoma and prostate tumor, respectively, are shown in **Figures 11 and 12**. In the microwave-based therapy the increased temperature is distributed in a much larger area compared to the NP-generated temperature.

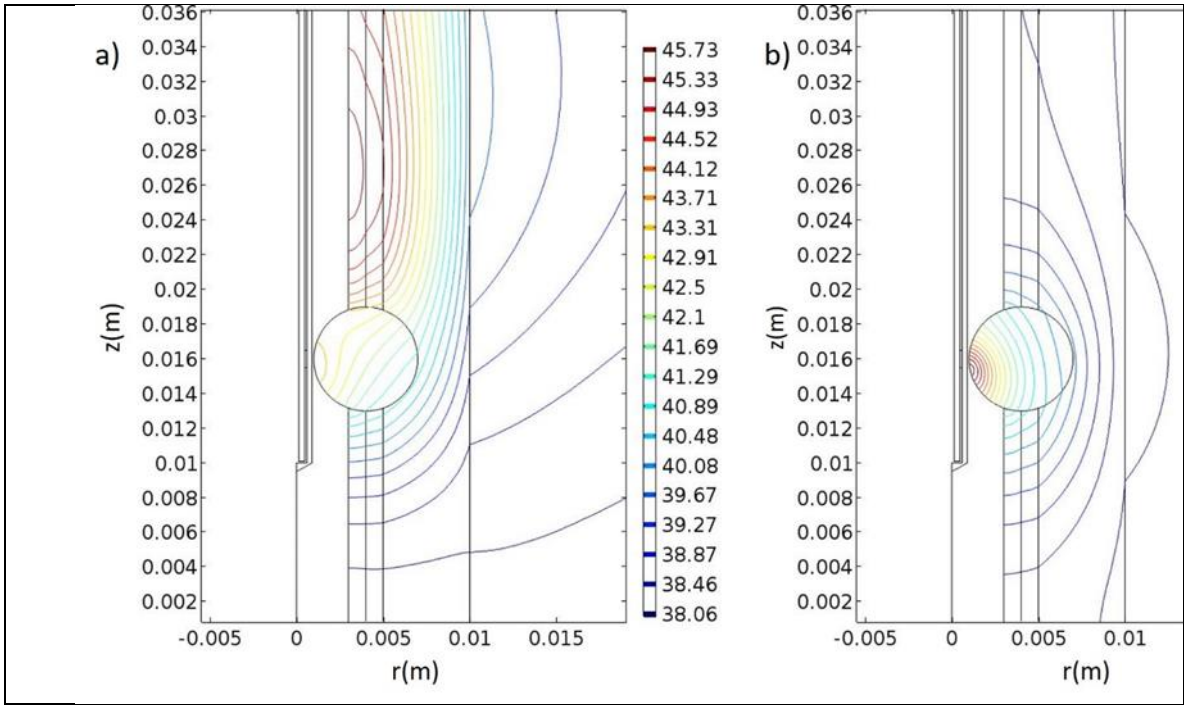

Figure 11. Simulation of microwave-induced temperature effects for melanoma tissue. (**a**) Temperature distribution at the 9th minute of treatment where the antenna is tuned at 2.4 GHz with power of 10W. (**b**) Temperature distribution at the 30th minute of heating and the antenna is tuned at 433 MHz with 100W power. The unit of the contours in Celsius degrees, and the unit of x and y axes in meters.

Specifically, in the melanoma when the antenna is tuned at 2.4 GHz at 10W **(Figure 11(a)),** the temperature can activate apoptotic mechanisms at the 9th minute of the therapy. When the antenna is set at 433 MHz ant 100 W (**Figure 11(b)**) at the 30th minute, the temperature is high enough to induce necrosis in the cells.

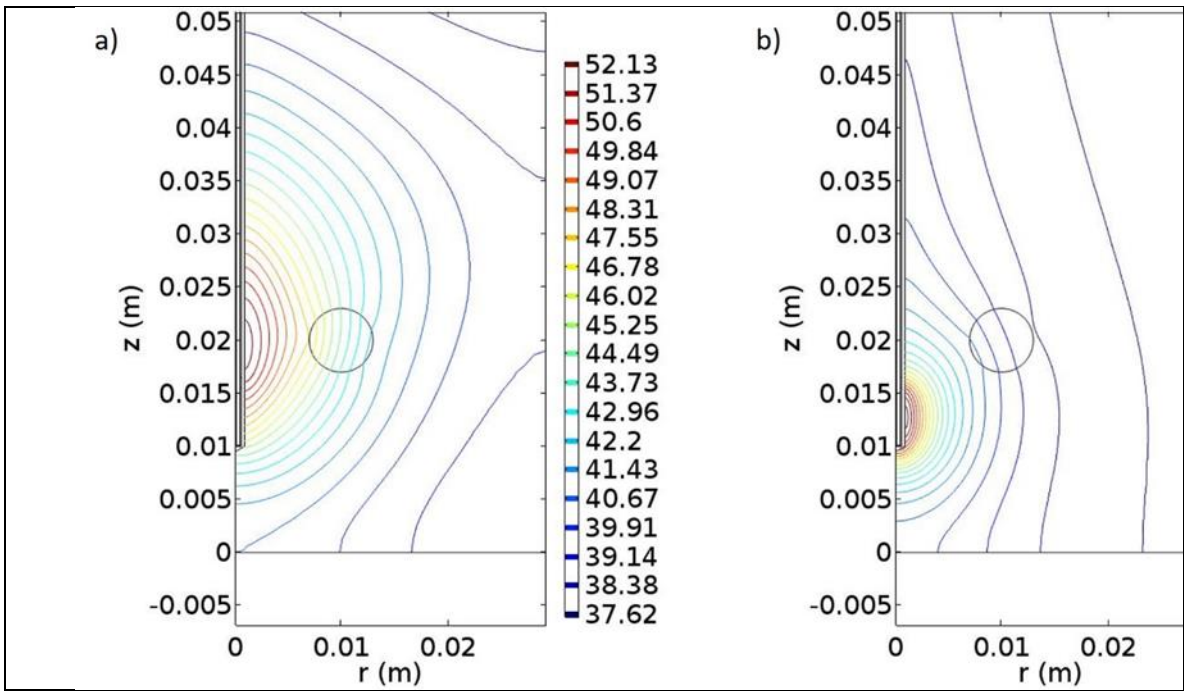

Figure 12. Simulation of microwave-induced temperature effects for prostate tissue. (**a**) Temperature distribution at the 9th minute of treatment where the antenna is tuned at 2.4 GHz with power of 10W. (**b**) Temperature distribution at the 30th minute of heating and the antenna was tuned at 433 MHz with power of 30W. The unit of the contours is in Celsius degrees, and the unit of x- and y-axes in meters.

In the prostate cancer, we followed the same procedures as in the case of melanoma. When the antenna was set at 2.4 GHz and 10 W the temperature that is generated is capable of inducing apoptotic mechanisms at the 9th minute of therapy, and when the antenna was set at 433 MHz and 30 W cell necrosis can begin at the 30th minute. Comparing the two frequencies, 2.4 GHz and 433 MHz, differences in the distribution of the temperature in the space could be observed.

On the second simulation case study, we present the tumor evolution over time for two cases: i) prostate cancer and ii) melanoma. Both tumor volumes are set at 113 mm^3. The temperature for the hyperthermic cell death of the prostate tumor is set at 50 ºC and 48 ºC for the melanoma. The use of the three-state model helps us observe the fast cell death during the first 30 minutes of heating for the melanoma and 15 minutes **(Figure 13(a))** prostate cancer **(Figure 13(c))**. After the treatment, the reduced viability due to the slow apoptotic cell death for the next 48 hours is shown in **Figures 13(b),-(d).** From the cell death and the tumor growth model, we obtained the evolution of tumor size during time (**Figure 15**). The results depicted in **Figure 15** indicate the reduction of tumor size when the patient receives therapy every 4 days for 7 sessions in Melanoma case, and in 0th, 2nd and then in 6th day in Prostate case. In the first two days of each 4-day interval the cells were damaged and underwent apoptotic cell death. In the next two days, the cancer cells recovered and started to proliferate again. This resulted to a slight increase on the tumor volume after the hyperthermic treatment.

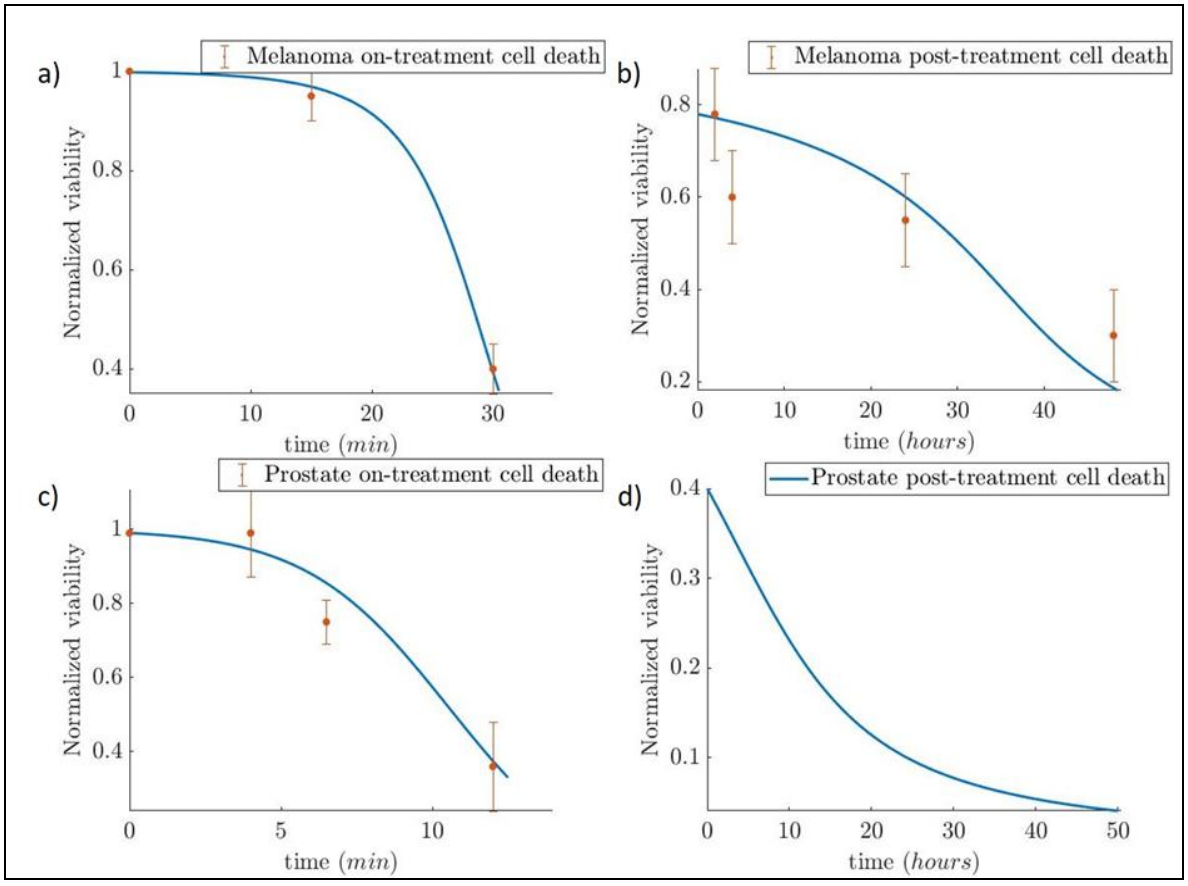

Figure 13. Simulation of tumor response to hyperthermia treatment. (a) and (**c**) depiction of the fast cell death that occurs during the treatment for melanoma and the prostate cancer cells. (**b)** and (**d**) depiction of post-treatment slow cell death for melanoma and the prostate cancer cell respectively.

The experimental data have been taken from Blanco-Andujar et al. [33] and Feng et al. [27] for melanoma, and Huang et al. [28] for the prostate cancer.

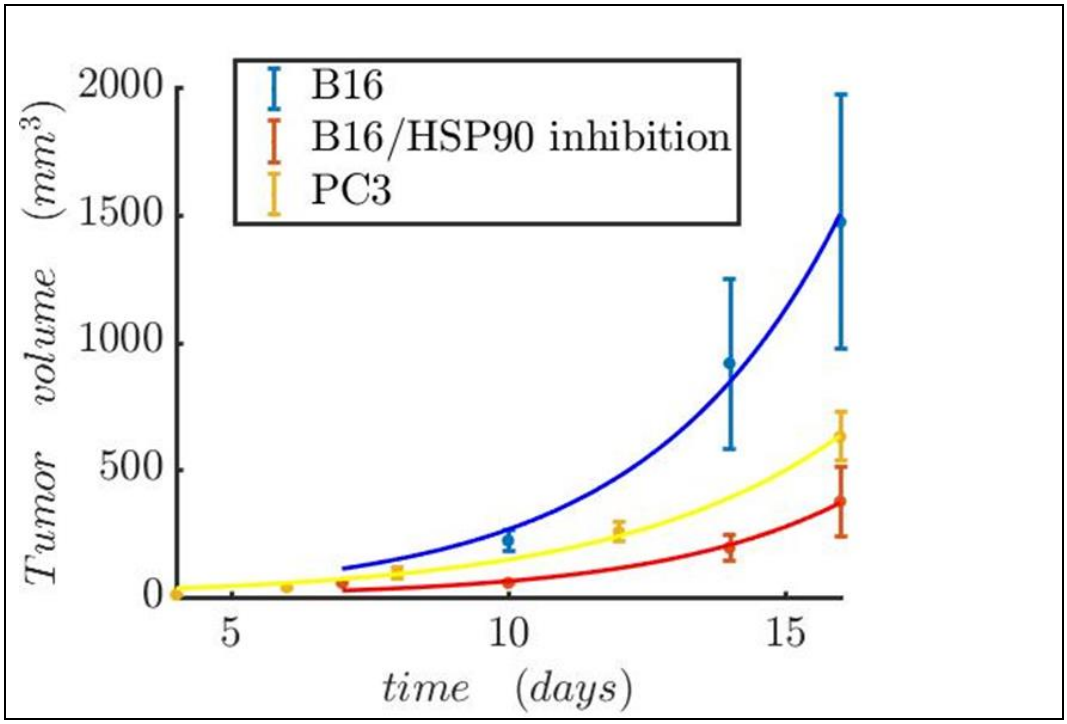

Figure 14. Tumor growth model. Prostate tumor growth in the absence of therapy and melanoma growth patterns both in the presence and absence of HSP90**.** The experimental data were taken from Proia et al. [29] for melanoma and Gao et al. [30] for the prostate cancer.

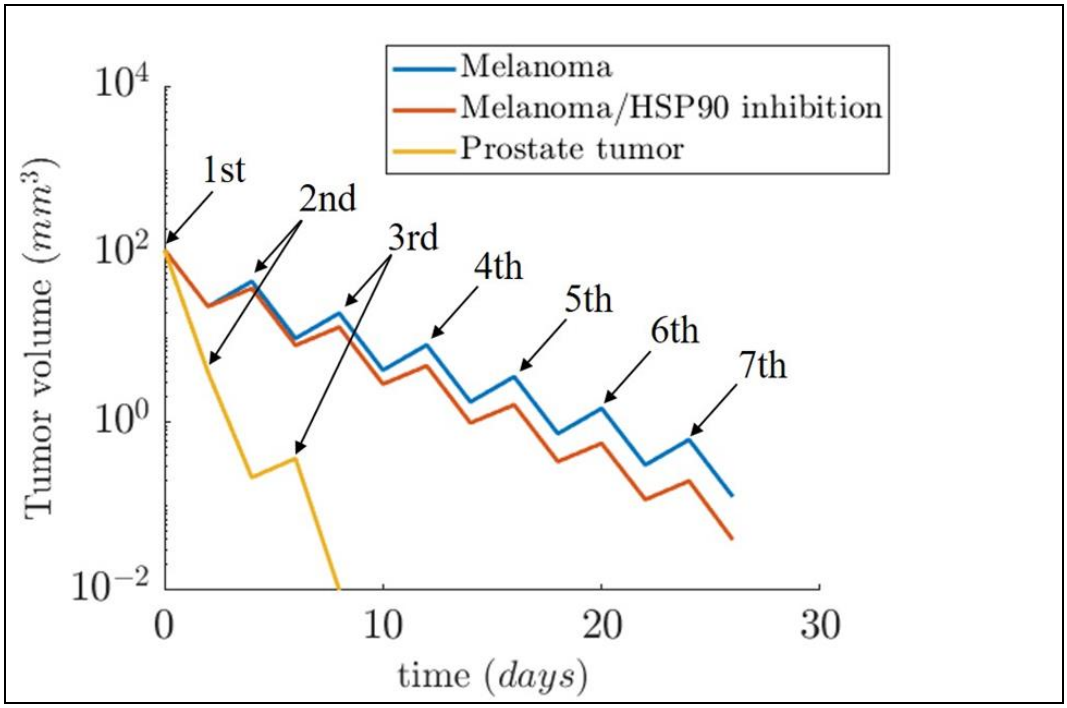

Figure 15. Estimated results for tumor shrinkage upon hyperthermia complete treatment (3-7 sessions) for two cancer types. The therapeutic sessions for Melanoma were repeated every 4 days. In the Prostate tumor the time interval between the first two sessions was 2 days, while the interval

between the 2nd and 3rd session was 4 days. For Melanoma, the expected values considering HSP90 inhibition were included.

4. Discussion

Simulations provide useful tools in cancer therapy based on their property to visualize and predict the phenomena that occur during cancer treatment (e.g. radiation effects), further enabling therapy optimization, in order to be as effective as possible and to minimize the side effects on the adjacent normal tissues. Microwave-induced hyperthermia is governed by physical mechanisms and effects that can be easily modeled because of the existing knowledge on electromagnetism and heat transfer effects.

In this simulation study, we present a hyperthermia treatment model mediated by Au-NPs which includes a prediction of the thermal effect on tumor evolution i.e. estimation of tumor shrinkage over time with the usage of mathematical models. We have performed also simulation of microwave-induced temperature effects for melanoma and prostate tissue and have demonstrated the presence of quantitative and qualitative differences between different types of tissues but with significant increases in temperatures above 50-60^{o}C in certain areas. Of importance, we deduced from this study that depending on the energy and frequency used, these temperature effects can be modulated in order to target specific tumor regions We also provide insights for a possible creation of a model for the role of HSP90 protein and potentially other HSPs. In the case of prostate tumors, we observed a much higher potency of HSP90 inhibition towards thermosensitization. Interestingly, in a very recent work it was exploited efficiently the knockdown of HSP70 and HSP90 by the use of gold nanorods loaded with HSP inhibitor-VER-155008 micelles for the destruction of colon cancer cells mediated by mild-temperature photothermal therapy [34].

Our findings revealed that the nanoparticle-induced hyperthermia has a more localized thermal effect, in the tumor tissue, as compared to the microwave-induced hyperthermia in the given frequencies. This result was expected, because the thermal profile is strongly correlated with the distribution and the density of the nanoparticles in the tumor tissue. On the other hand, differences in penetration depth among the two frequencies were observed. Microwave-induced hyperthermia, as it is currently applied, lacks the ability of precise heat localization compared to the nanoparticle-induced hyperthermia. The current version can be improved by the implantation of iron oxide nanoparticles that can enhance the heat effect in tumor tissue.

The findings of the present study could be exploited towards the design of anti-neoplastic therapeutic strategies, where radiation/NP-induced thermotherapy and simultaneous pharmacologic inhibition of molecular chaperones (HSPs) could be utilized to both sensitize resistant cancer cells to death and also increase their immunological potential. For example, hypoxia related studies have shown that in breast cancer cells the uptake of NPs was increased in hypoxic microenvironments, as compared to normoxic conditions in head and neck squamous cell carcinoma (HNSCC) cells [35].

Acknowledgements: Dr. A.G. Georgakilas acknowledges funding from the DAAD Grant "DNA Damage and Repair and Their Relevance to Carcinogenesis" (No 57339330). I Tremi's Doctoral Dissertation is funded by the State Scholarship Foundation (IKY) within the act "STRENGTHENING HUMAN RESEARCH POTENTIAL THROUGH THE DOCTORAL IMPLEMENTATION RESEARCH", from the resources of "Human Resources Development, Education and Lifelong Learning", 2014-2020.

Conflict of Interest: The authors declare no conflict of interest.

References

1. Pavlopoulou, A.; Bagos, P.G.; Koutsandrea, V.; Georgakilas, A.G. Molecular determinants of radiosensitivity in normal and tumor tissue: A bioinformatic approach. *Cancer Letters* **2017**, *403*, 37-47, doi:https://doi.org/10.1016/j.canlet.2017.05.023.
2. Dewhirst, M.W.; Vujaskovic, Z.; Jones, E.; Thrall, D. Re-setting the biologic rationale for thermal therapy. *International Journal of Hyperthermia* **2005**, *21*, 779-790, doi:10.1080/02656730500271668.
3. Dimitriou, N.M.; Tsekenis, G.; Balanikas, E.C. Gold nanoparticles, radiations and the immune system: current insights into the physical mechanisms and the biological interactions of this new alliance towards cancer therapy. *Pharmacology & therapeutics* **2017**.
4. Cherukuri, P.; Glazer, E.S.; Curley, S.A. Targeted hyperthermia using metal nanoparticles. *Advanced Drug Delivery Reviews* **2010**, *62*, 339-345, doi:http://dx.doi.org/10.1016/j.addr.2009.11.006.
5. Keisari, Y. Tumor abolition and antitumor immunostimulation by physico-chemical tumor ablation. *Frontiers in bioscience* **2017**, *22*, 310-347.
6. Jondal, D.E.; Thompson, S.M.; Butters, K.A.; Knudsen, B.E.; Anderson, J.L.; Carter, R.E.; Roberts, L.R.; Callstrom, M.R.; Woodrum, D.A. Heat Stress and Hepatic Laser Thermal Ablation Induce Hepatocellular Carcinoma Growth: Role of PI3K/mTOR/AKT Signaling. *Radiology* **2018**, 10.1148/radiol.2018172944, 172944, doi:10.1148/radiol.2018172944.
7. Soni, S.; Tyagi, H.; Taylor, R.A.; Kumar, A. Investigation on nanoparticle distribution for thermal ablation of a tumour subjected to nanoparticle assisted thermal therapy. *Journal of Thermal Biology* **2014**, *43*, 70-80, doi:https://doi.org/10.1016/j.jtherbio.2014.05.003.
8. Vriend, L.E.M.; van den Tempel, N.; Oei, A.L.; L'Acosta, M.; Pieterson, F.J.; Franken, N.A.P.; Kanaar, R.; Krawczyk, P.M. Boosting the effects of hyperthermia-based anticancer treatments by HSP90 inhibition. *Oncotarget* **2017**, *8*, 97490-97503, doi:10.18632/oncotarget.22142.
9. Mie, G. Beiträge zur Optik trüber Medien, speziell kolloidaler Metallösungen (Contributions to the optics of turbid media, especially colloidal metal suspensions). *Ann. Phys. (Leipzig)* **1908**, *25*, 377-445.
10. Ellis, R.J.; Hartl, F.U. Principles of protein folding in the cellular environment. *Current opinion in structural biology* **1999**, *9*, 102-110.
11. Calderwood, S.K.; Murshid, A. Molecular Chaperone Accumulation in Cancer and Decrease in Alzheimer's Disease: The Potential Roles of HSF1. *Frontiers in neuroscience* **2017**, *11*, 192, doi:10.3389/fnins.2017.00192.
12. Kroemer, G.; Galluzzi, L.; Kepp, O.; Zitvogel, L. Immunogenic cell death in cancer therapy. *Annual review of immunology* **2013**, *31*, 51-72, doi:10.1146/annurev-immunol-032712-100008.
13. O'Neill, D.P.; Peng, T.; Stiegler, P.; Mayrhauser, U.; Koestenbauer, S.; Tscheliessnigg, K.; Payne, S.J. A Three-State Mathematical Model of Hyperthermic Cell Death. *Annals of biomedical engineering* **2011**, *39*, 570-579, doi:10.1007/s10439-010-0177-1.
14. Benzekry, S.; Lamont, C.; Beheshti, A.; Tracz, A.; Ebos, J.M.L.; Hlatky, L.; Hahnfeldt, P. Classical Mathematical Models for Description and Prediction of Experimental Tumor Growth. *PLOS Computational Biology* **2014**, *10*, e1003800, doi:10.1371/journal.pcbi.1003800.
15. Tuersun, P.; Han, X.e. Optical absorption analysis and optimization of gold nanoshells. *Appl. Opt.* **2013**, *52*, 1325-1329, doi:10.1364/AO.52.001325.
16. Keribig, U.; Vollmer, M. *Optical Properties of Metal Clusters*; Springer: 2015.
17. Averitt, R.D.; Westcott, S.L.; Halas, N.J. Linear optical properties of gold nanoshells. *J. Opt. Soc. Am. B* **1999**, *16*, 1824-1832, doi:10.1364/JOSAB.16.001824.
18. https://refractiveindex.info/. Availabe online: (accessed on

19. Refractive index database. Avaliable online: https://refractiveindex.info/.
20. Rakić, A.D.; Djurišić, A.B.; Elazar, J.M.; Majewski, M.L. Optical properties of metallic films for vertical-cavity optoelectronic devices. *Appl. Opt.* **1998**, *37*, 5271-5283, doi:10.1364/AO.37.005271.
21. Qian, L.P.; Zhou, L.H.; Too, H.-P.; Chow, G.-M. Gold decorated NaYF4:Yb,Er/NaYF4/silica (core/shell/shell) upconversion nanoparticles for photothermal destruction of BE(2)-C neuroblastoma cells. *Journal of Nanoparticle Research* **2011**, *13*, 499-510, doi:10.1007/s11051-010-0080-6.
22. Ali, M.Y.; Grimm, C.F.; Ritter, M.; Mohr, L.; Allgaier, H.-P.; Weth, R.; Bocher, W.O.; Endrulat, K.; Blum, H.E.; Geissler, M. Activation of dendritic cells by local ablation of hepatocellular carcinoma. *Journal of hepatology* **2005**, *43*, 817-822, doi:https://doi.org/10.1016/j.jhep.2005.04.016.
23. Rai, N.K.; Rai, K.S. Effect of metabolic heat generation and blood perfusion on the heat transfer in the tissues with a blood vessel. *Heat and Mass Transfer* **1999**, *35*, 75-79, doi:10.1007/s002310050300.
24. Gowrishankar, T.R.; Stewart, D.A.; Martin, G.T.; Weaver, J.C. Transport lattice models of heat transport in skin with spatially heterogeneous, temperature-dependent perfusion. *Biomedical engineering online* **2004**, *3*, 42, doi:10.1186/1475-925X-3-42.
25. Jiao, J.; Guo, Z. Thermal interaction of short-pulsed laser focused beams with skin tissues. *Physics in medicine and biology* **2009**, *54*, 4225-4241, doi:10.1088/0031-9155/54/13/017.
26. Cornelissen, L.H.; Bronneberg, D.; Oomens, C.W.J.; Baaijens, F.P.T. Diffusion measurements in epidermal tissues with fluorescent recovery after photobleaching. *Skin Research and Technology* **2008**, *14*, 462-467, doi:doi:10.1111/j.1600-0846.2008.00313.x.
27. Feng, Y.; Oden, J.T.; Rylander, M.N. A Two-State Cell Damage Model Under Hyperthermic Conditions: Theory and In Vitro Experiments. *Journal of biomechanical engineering* **2008**, *130*, 041016-041016, doi:10.1115/1.2947320.
28. Huang, H.-C.; Rege, K.; Heys, J.J. Spatiotemporal Temperature Distribution and Cancer Cell Death in Response to Extracellular Hyperthermia Induced by Gold Nanorods. *ACS nano* **2010**, *4*, 2892-2900, doi:10.1021/nn901884d.
29. Proia, D.A.; Kaufmann, G.F. Targeting Heat-Shock Protein 90 (HSP90) as a Complementary Strategy to Immune Checkpoint Blockade for Cancer Therapy. *Cancer Immunology Research* **2015**, *3*, 583-589, doi:10.1158/2326-6066.cir-15-0057.
30. Gao, F.; Al-Azayzih, A.; Somanath, P.R. Discrete functions of GSK3α and GSK3β isoforms in prostate tumor growth and micrometastasis. *Oncotarget* **2015**, *6*, 5947-5962, doi:10.18632/oncotarget.3335.
31. Zuber, A.; Purdey, M.; Schartner, E.; Forbes, C.; van der Hoek, B.; Giles, D.; Abell, A.; Monro, T.; Ebendorff-Heidepriem, H. Detection of gold nanoparticles with different sizes using absorption and fluorescence based method. *Sensors and Actuators B: Chemical* **2016**, *227*, 117-127, doi:https://doi.org/10.1016/j.snb.2015.12.044.
32. Sambou, A.; Ngom, B.D.; Gomis, L.; Beye, A.C. Turnability of the Plasmonic Response of the Gold Nanoparticles in Infrared Region. *American Journal of Nanomaterials* **2016**, *4*, 63-69, doi:10.12691/ajn-4-3-3.
33. Blanco-Andujar, C.; Ortega, D.; Southern, P.; Nesbitt, S.A.; Thanh, N.T.K.; Pankhurst, Q.A. Real-time tracking of delayed-onset cellular apoptosis induced by intracellular magnetic hyperthermia. *Nanomedicine* **2015**, *11*, 121-136, doi:10.2217/nnm.15.185.
34. Tang, X.; Tan, L.; Shi, K.; Peng, J.; Xiao, Y.; Li, W.; Chen, L.; Yang, Q.; Qian, Z. Gold nanorods together with HSP inhibitor-VER-155008 micelles for colon cancer mild-temperature photothermal therapy. *Acta*

Pharmaceutica Sinica B **2018**, https://doi.org/10.1016/j.apsb.2018.05.011, doi:https://doi.org/10.1016/j.apsb.2018.05.011.

35. Chen, E.Y.; Hodge, S.; Tai, K.; Hou, H.; Khan, N.; Hoopes, P.J.; Samkoe, K.S. Oxygen microenvironment affects the uptake of nanoparticles in head and neck tumor cells. *Proceedings of SPIE--the International Society for Optical Engineering* **2013**, *8584*, 85840F, doi:10.1117/12.2008067.